Search for the second forbidden β decay of ^{8}B to the ground state of ^{8}Be

M. K. Bacrania,* N. M. Boyd,† R. G. H. Robertson, and D. W. Storm
Center for Experimental Nuclear Physics and Astrophysics, Physics Department, University of Washington, Seattle, Washington 98195, USA
(Received 20 August 2007; published 28 November 2007)

A significant decay branch of ^{8}B to the ground state of ^{8}Be would extend the solar neutrino spectrum to higher energies than anticipated in the standard solar models. These high-energy neutrinos would affect current neutrino oscillation results and also would be a background to measurements of the hep process. We have measured the delayed α particles from the decay of ^{8}B, with the goal of observing the two 46-keV α particles arising from the ground-state decay. The ^{8}B was produced using an in-flight radioactive beam technique. It was implanted in a silicon PIN-diode detector that was capable of identifying the α particles from the ^{8}Be ground state. From this measurement we find an upper limit (at 90% confidence level) of 7.3×10^{-5} for the branching ratio to the ground state. In addition to describing this measurement, we present a theoretical calculation for this branching ratio.

DOI: 10.1103/PhysRevC.76.055806 PACS number(s): 23.40.Bw, 23.60.+e, 26.65.+t

I. INTRODUCTION

There have been several experiments [1–3] conducted recently to measure the α-particle spectrum following the allowed (2^+ to 2^+) β decay of ^{8}B to the broad first excited state at 3 MeV in ^{8}Be. The neutrinos from this decay provide the signal for solar neutrino measurements, such as those made at the Sudbury Neutrino Observatory (SNO) and the Super-Kamiokande detector; and precise knowledge of their spectrum at creation, combined with accurate measurements in the solar neutrino detectors, is important for understanding neutrino oscillations. The only higher energy neutrinos from the Sun come from the hep process [4] (weak capture of a proton by ^{3}He producing $e^+ + \nu$), expected to be at a rate roughly 10^{-3} of the ^{8}B neutrinos, and from the second forbidden (2^+ to 0^+) decay of ^{8}B to the ground state of ^{8}Be. Specifically these reactions are

$$^3\mathrm{He} + p \rightarrow {}^4\mathrm{He} + e^+ + \nu + 18.77\ \mathrm{MeV}$$

and

$$^8\mathrm{B} \rightarrow {}^8\mathrm{Be} + e^+ + \nu + 16.95\ \mathrm{MeV}.$$

An ft value for the latter decay, estimated using $\log_{10} ft = 13.3$ obtained from the 2^+ to 0^+ decay of ^{36}Cl, suggests the ^{8}B 2^+ to 0^+ decay should have a branching ratio of order only 10^{-7}. The ^{8}B decay has an unusually large energy, and second forbidden decays should have an extra factor of k^2 (k is the momentum transfer to the leptons) in their decay rate. Comparing the square of the endpoint energy for ^{8}B with that for ^{36}Cl suggests an additional factor of 570 in the rate for the second forbidden decay of ^{8}B. This rate would correspond to a $\log_{10} ft$ of 10.5, a value still in the expected range for second forbidden transitions. The corresponding branching ratio would be 3×10^{-5}. If the branching ratio were as large as about 1%, it would contribute significantly to the neutrino spectrum observed at SNO.

Decay to the ground state of ^{8}Be is difficult to measure, since that state decays to two α particles producing only 92 keV. We are unaware of previous attempts to measure this branch. Published estimates range from 3×10^{-6} [5] to $O(10^{-4})$ [6,7]. The latter estimate includes only the vector contribution to the second forbidden decay. In this paper, we describe the technique of our measurement, give the result, and present theoretical calculations based on the shell model and on measured γ-ray transition matrix elements.

II. EXPERIMENT

We made a ^{8}B beam using an in-flight production technique. The ^{8}B were implanted in a silicon detector that was capable of measuring the energy from the delayed α decay of the ^{8}Be ground state, as well as from most of the spectrum of the delayed α decay of the ^{8}Be first excited state. The decays were tagged by detecting the decay positrons in a scintillator. The silicon detector was calibrated using backscattered α particles of known energy and delayed α decays of implanted ^{12}N.

A. Radioactive beams

The ^{8}B for implantation in the detector was made using the ^{3}He(^{6}Li,^{8}B)n reaction. A 32-mm-diameter gas cell was located at the focal point of the analyzing magnet of the University of Washington tandem accelerator. This gas cell had entrance and exit windows of 2.5-μm Havar [8] and contained ^{3}He at about 0.6 bar. The incident beam was 24-MeV ^{6}Li, which, after accounting for energy loss in the windows and gas, produced ^{8}B in the forward direction with an energy centered at 15.5 MeV and a spread of 1.1 MeV, resulting from energy loss in the gas.

The beam transport following the analyzing magnet consisted of a 30° switching magnet followed by a quadrupole doublet. These elements are normally used to focus the analyzed beam from the accelerator onto the target in the

*Presently at Nuclear Safeguards Science and Technology, Los Alamos National Laboratory, Los Alamos, NM 87544, USA.

†Presently at Department of Physics and Astronomy, University of British Columbia, Vancouver, BC V6T 1Z1, Canada.

scattering chamber. For the present experiment, we had to optimize the capture and transport of the radioactive beam through the 20-mm aperture for our detector, which was located at the target position in the scattering chamber. Using TRANSPORT [9] and TURTLE [10] codes, we found that this could be done by first tuning the beamline following the gas cell appropriately for transport of a straight-going monoenergetic beam of the desired magnetic rigidity, and then by increasing the quadrupole strength by about 10%. The energy acceptance of this system was only about 2%, which is less than the energy spread resulting from the gas cell, so there was no reason to have either a bigger cell or denser gas. We tuned the radioactive beam transport elements by tuning first a 7.44-MeV $^{6}Li^{3+}$ beam (matching the 15.5-MeV $^{8}B^{5+}$ radioactive beam in magnetic rigidity) through a small aperture. Then, while irradiating the gas cell with the 24-MeV ^{6}Li beam, we monitored the ^{8}B implantation rate and increased the quadrupole current to maximize the rate. We also swept the switching magnet field, which we monitored with a Hall probe, to make sure we were accepting the central energy from the gas cell.

As the rigidity of the primary beam is higher than that of the radioactive beam, a degraded primary beam is a serious contaminant. To minimize degradation of the primary beam after the analyzing magnet, we regulated the accelerator voltage with the generating voltmeter regulator [11] and completely retracted the beam regulation slits located downstream of the analyzing magnet. Particular attention had to be paid to the beam tuning in order to minimize the amount of beam striking other limiting apertures in the beamline.

In addition to the ^{8}B beam, we produced a ^{12}N beam for calibration of the silicon detector. This beam was made using the ^{3}He(^{10}B,^{12}N)n reaction, with a 35-MeV ^{10}B beam, producing 24.2-MeV $^{12}N^{7+}$, in an analogous manner. The ^{12}N energy was chosen to produce the same implantation depth for the ^{12}N as for the ^{8}B. The choice of the ^{12}N charge state was determined by the background, because the most probable charge state of ^{12}N, 6+, was too close in rigidity to the ^{10}B primary beam. Using the coincidence with the scintillator, we were able to tag about 3–5 ^{8}B/s with 170–330 pnA of ^{6}Li, and about 0.5–1 ^{12}N/s with 50–100 pnA of ^{10}B. For the ^{8}B beam, the background in the silicon detector, primarily consisting of degraded ^{6}Li from the primary beam, was 0.6–1 kHz. For the ^{12}N beam, the degraded ^{10}B background was 2 kHz. This background rate in our detector set an intensity limit for the primary beam.

B. Detector

The detector assembly consisted of a 500-μm thick by 18-mm square Hamamatsu S-3204-06 PIN diode [12], in front of which was a 51-mm cube of Bicron-400 scintillator with a 20-mm-diameter hole on the beam axis. A 6.4-mm-thick lead shield with a 17-mm-diameter aperture was placed in front of the scintillator, and the scintillator was coupled on the side to a photomultiplier tube. This thickness of lead was sufficient to absorb positrons from decaying ^{8}B that stopped on it. Ions that passed through the lead aperture would stop in the PIN diode, and were not able to hit the sides of the hole in the scintillator.

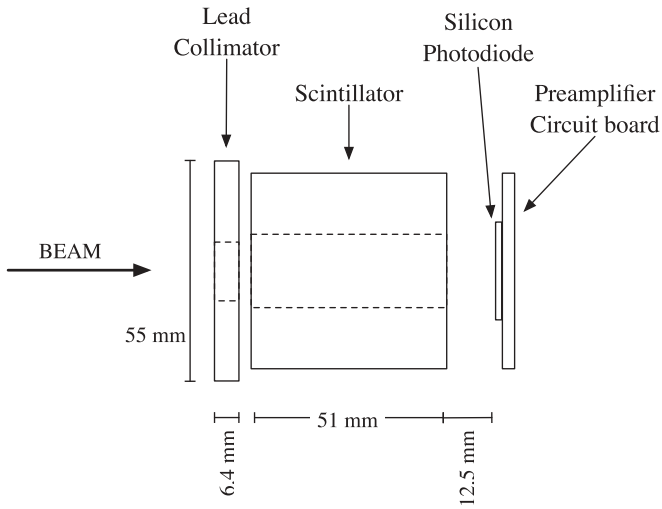

FIG. 1. Schematic of the detector assembly. The various hole diameters are given in the text. The cooled copper mount (not shown) was located behind the preamplifier circuit board.

The 15-MeV ^{8}B ions were implanted approximately 20 μm into the silicon, and about 20% of the decays produced positrons that would enter the scintillator, tagging the decay. To minimize distortions in the α-particle spectrum from positron energy deposition, the scintillator detector was placed in front of the silicon detector, thus minimizing the track length of the tagged positrons in the silicon detector. Tagging with positrons that passed through the silicon detector was not practical, as their energy deposition would be larger than the energy from the decay from the ^{8}B ground state. Indeed, as discussed in Sec. II D2, positrons that scatter through large angles affect the efficiency of the detection. The PIN diode was mounted on a custom charge-sensitive preamplifier [13] built on a 5-cm-square circuit board. The preamplifier and detector were cooled by a thermoelectric cooler coupled to a 19-mm-wide and 3-mm-thick copper strip that ran the height of the preamplifier circuit board. This assembly is shown in Fig. 1.

When cooled to 10°C, the measured leakage current of a new PIN diode was typically 10–12 nA. The resolution (full width at half maximum, FWHM) was 7.8 keV for 81-keV γ rays, and a threshold about 30 keV was practical. During experimental runs, the reverse current would rise to 30–60 nA after 2 weeks of irradiation, at which point the resolution would decrease to approximately 10 keV at 81 keV.

C. Electronics and data acquisition

The photomultiplier on the scintillation detector produced both a timing and a pulse-height signal. The timing signal started a time-to-amplitude converter (TAC). The output of the charge-sensitive preamplifier for the silicon diode detector was split into two channels, each with an Ortec 572 amplifier. The maximum range of the *high gain* channel corresponded to about 1 MeV, while the maximum observable energy in the

low gain channel was 8 MeV. The two unipolar signals were digitized, as was the pulse-height signal from the scintillator. The bipolar outputs of the amplifiers for the silicon detector generated timing signals, which were combined in an OR module, and the resulting logic signal was delayed and used to trigger the data acquisition system (DAQ), contained in a single computer-automated measurement and control (CAMAC) crate. A parallel output of the OR unit was used to stop the TAC, which was started by the signal from the scintillator. This TAC signal was also digitized. Thus any signal over the 30-keV threshold from the silicon detector would trigger the DAQ, while a coincidence (within a 5-μs time window) would also produce a TAC output. The threshold on the scintillator was set high enough that its rate was substantially lower than that in the silicon diode detector. The DAQ system was operated in event mode, with two silicon detector energy signals, one scintillator pulse height, and one timing signal per event.

A precision pulser, coupled to the silicon detector preamplifier, was used for monitoring dead time and amplifier gain shifts. A scaler module was used to count pulser triggers, pulses from the beam-current integrator, the number of TAC outputs, and the number of DAQ triggers. The pulser and the electronics feeding the DAQ system were located in a temperature-stabilized rack, which was controlled to within $\pm 0.1^{\circ}$C. During regular data taking, the pulser was set to correspond to about a 0.5-MeV signal in the silicon detector. The DAQ CAMAC crate was located in the temperature-controlled electronics rack and controlled by a Wiener CC32 peripheral component interconnect (PCI) crate controller [14]. For data acquisition, initially we used the JAVA-based JAM [15] system, but subsequently switched to the Objective-C-based ORCA [16] system.

The gain stability of the silicon-detector preamplifier and associated electronics was monitored by observing the pulser signal in the high- and low-gain channels. Also, the irradiations were stopped at hourly intervals, and a measurement of the pulser spectrum for various settings of the pulser attenuation circuit was made ($1.0\times$, $0.5\times$, $0.2\times$, $0.1\times$). These measurements allowed the monitoring of both gain and linearity as a function of irradiation time.

From the event-mode data, singles histograms of the silicon-detector energy spectra, the TAC signals, and the scintillator pulse height were formed. Prompt coincident events were retained by applying cuts (discussed in Sec. III) to the TAC and scintillator spectra.

D. Calibration

1. Silicon-detector energy calibration

The energy calibration for the $^{8}\mathrm{B}(2^{+}) \rightarrow {}^{8}\mathrm{Be}(0^{+})$ decay measurement was obtained from a ^{133}Ba radioactive source, which produces a number of low-energy γ-ray lines between 80 and 400 keV. These photons convert by Compton scattering and the photoelectric effect in the silicon. In contrast, measurement of the $^{8}\mathrm{B}(2^{+}) \rightarrow {}^{8}\mathrm{Be}(0^{+})$ decay rate involved the detection of two low-energy α particles, which directly ionize the detector medium. The ionization energy for γ rays in silicon, 3.68 ± 0.02 eV, is larger than the ionization energy for α particles in silicon, 3.62 ± 0.02 eV. This difference, a ratio of 1.017 ± 0.008, must be accounted for when relating a calibration obtained from γ rays to the measured α-particle energy spectrum [17]. In addition, the fractional loss of energy to non-ionizing processes increases as the α-particle incident energy decreases; this *pulse-height defect* goes undetected by the silicon detector.

Tabulated values of the expected nuclear and total stopping powers have been published in Ref. [18]. At low energies, these tabulated nuclear stopping powers are calculated via a model, because available experimental data are limited. To determine the expected pulse height of the $^{8}\mathrm{B}(2^{+}) \rightarrow {}^{8}\mathrm{Be}(0^{+})$ decay signal reliably, it was necessary to measure the pulse-height defect of α particles in our silicon detector.

The uncertainty in the ionization energy ratio affects the determination of the pulse-height defect, but, as will be seen below, the calibration of the low-energy α particles is not affected by it. Thus we divide the calibration obtained from ^{133}Ba by 1.017 to get the corresponding calibration for α particles without the pulse-height deficit, and these energies are used for our calibrations. The pulse-height deficit (with uncertainties) is applied subsequently.

To measure the pulse-height defect of low-energy α particles in silicon, ^{4}He ions were produced at eight different energies from 90 to 475 keV using the UW tandem accelerator with the terminal ion source. These α particles were backscattered from a gold monolayer evaporated on a 50-μg/cm^2 carbon target foil into the collimated silicon detector located at 100°. As the energy the particles deposit in the active part of the detector is reduced from the incident energy by the SiO_2 dead layer on the front of the detector, it was necessary to quantify the energy loss in the dead layer. This was done by repeating the measurements for each incident energy with the detector face angled at numerous positions between -45° and $+45^{\circ}$ to the scattering axis. At each angle, the effective thickness of the dead layer through which the particles passed is $\Delta x / \cos\theta$, where Δx is the physical dead-layer thickness. The value of Δx was determined by combining all the measured results and performing a global fit to the measured energy (as determined from the ^{133}Ba calibration, adjusted by the ratio of ionization energy for electrons and α particles) vs the detector angular position. From this series of experiments, the pulse-height defect was found to vary from 7.9 ± 0.3 to 11.4 ± 0.7 keV for α-particle incident energies in the active part of the detector varying from 55.9 to 391.4 keV. The measured energy loss in the dead layer corresponded to 43.1 ± 0.4 μg/cm^2 of SiO_2. There is an additional systematic uncertainty of 0.8% in these pulse-height defects, arising from the uncertainty in the ratio of ionization energy for α particles to that for photons [17].

The low-energy α calibration, including corrections for pulse-height defect and for the ratio of ionization energy for electrons and α particles, was cross-checked using the decay of implanted ^{12}N, which β decays to the 7.65-MeV state of ^{12}C, which then decays to three α particles with a total energy release of 379 keV.

Two of the α particles come from the breakup of the ground state of ^{8}Be. By comparing the known energy of this decay (accounting for decay kinematics, discussed in the following

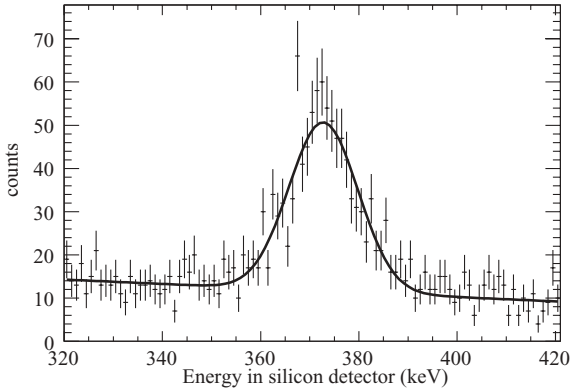

FIG. 2. ^{12}N 3α decay peak observed in the high-gain channel, fit with a Gaussian peak on a linear background. The energy deposited, including recoil and positron summing, is predicted to be 388.5 $\pm$ 1.2 keV from our Monte Carlo simulations. The center of the peak appears at 372.5 $\pm$ 3.0 keV, indicating a total 16 $\pm$ 3 keV pulse-height defect.

section) to the detected energy deposition, we were able to determine the pulse-height defect independently, assuming that the energy dependence of the pulse-height defect was that given by the predicted non-ionizing stopping power [18]. The spectrum obtained from the ^{12}N decay is shown in Fig. 2. The results of the ^{12}N decay and the single α-particle measurements are shown in Fig. 3, along with the predicted pulse-height defect obtained from Ref. [18]. The pulse-height defect obtained from the single α-particle measurement is calculated to be 7.5 $\pm$ 0.3 keV at 46 keV. On the other hand, the pulse-height defect from the ^{12}N decay measurement is found to be 4.5 $\pm$ 0.9 keV at 46 keV. We use these two values as lower and upper bounds when constructing the energy window for the expected signature from ^{8}B decay.

As the low-energy α calibration includes corrections for both pulse-height defect and the ratio of ionization energies, and as the former is obtained using the latter, uncertainties in this ratio will cancel in the calibration for the ^{8}B measurement.

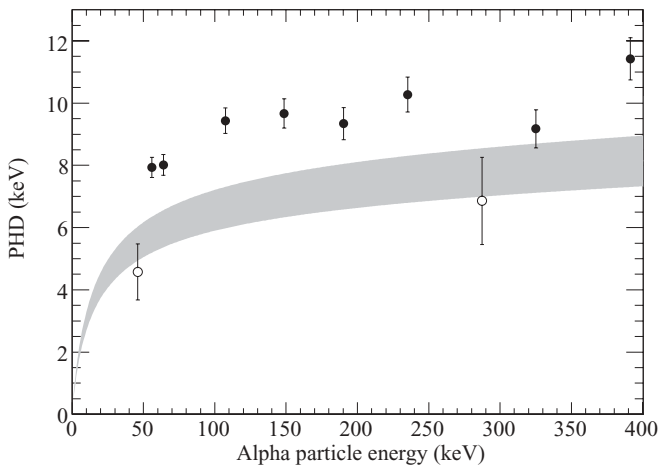

FIG. 3. Pulse-height defect (PHD) measured using single α particles (solid circles) and from ^{12}N decay (open circles). The shaded band is the PHD value obtained from integrating the stopping-power tables in Ref. [18], including a 10% uncertainty.

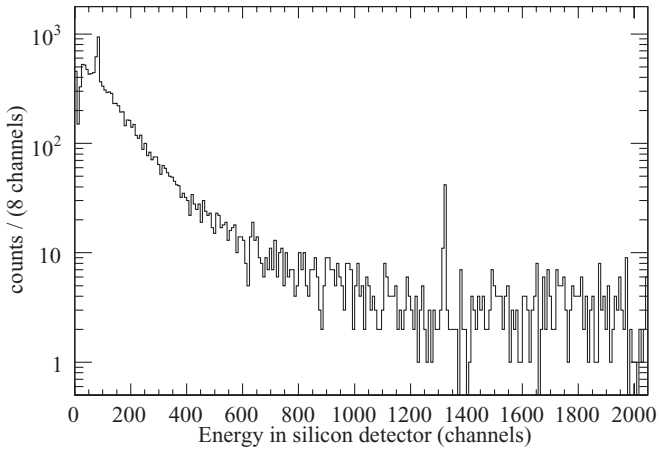

FIG. 4. ^{12}N spectrum observed in the low-gain channel. The peaks near channels 80 and 1300 correspond to total energies from 3α decay of 388.5 $\pm$ 1.2 and 5443 $\pm$ 6 keV, respectively, including recoil and positron summing. The continuum is dominated by positrons backscattering from the detector mount and thus passing through the detector twice. In ^{12}N decay, only 3% of the positrons are accompanied by α particles.

The photons are just an intermediate calibration. The determination of the pulse-height defect links a known α-particle energy to a photon energy, and then the use of that photon for calibrating the measurement of ^{8}B establishes that calibration in terms of the known α-particle energy.

The low-gain channel, which contained the ^{8}B(2+) $\rightarrow$ ^{8}Be(2+) decays, was calibrated using the two lines from ^{12}N decay, resulting from the 3α decay of the ^{12}C levels at 7.65 and 12.71 MeV. These are illustrated in Fig. 4. The energies of these lines were adjusted for positron summing, ^{12}C recoil, and pulse-height defect.

2. Recoil and energy deposition calculations

Two corrections are required for the analysis of both ^{8}B and ^{12}N energy spectra: the recoil energy imparted by the leptons to the daughter nucleus, and the amount of energy deposited in the silicon detector by the outgoing positron. As a result of the high decay energy, a significant amount of recoil energy (up to 19 keV) can be imparted to the ^{8}Be daughter nuclei by the outgoing leptons, resulting in an overall broadening of the energy window in which the decay signal is expected to lie. The ^{12}C daughters receive less recoil energy (up to 3.3 keV). Using the predictions of the positron-neutrino correlation from the calculations described in Sec. IV, we found a distribution of recoil energy between 0 and 19 keV for the ^{8}B(2^{+}) $\rightarrow$ ^{8}Be(0^{+}) decay, which was peaked near the maximum energy. The Gamow-Teller decay of ^{12}N yields a fairly uniform distribution of recoil energy between 0 and 3.3 keV.

The additional energy deposited by the escaping positron adds to the decay energy and results in an overall energy shift. We minimized the magnitude of this energy shift by implanting the ^{8}B and ^{12}N ions near the upstream surface of the silicon detector. The distribution of the positron energy deposition

was computed by Monte Carlo simulation, using measured stopping powers from Ref. [18]. The ^{8}B and ^{12}N implantation depths, 20.2 ± 0.3 and $18.7 \pm 1.5 \mu$m, respectively, were obtained from Ref. [19]. The simulated energy distributions were fit with a Landau distribution, and the most likely energy deposition for positrons coming from $^8\mathrm{B}(2^+) \rightarrow {}^8\mathrm{Be}(0^+)$ and ^{12}N decay was 9.5 ± 0.9 and 7.8 ± 0.6 keV, respectively.

A significant number of positrons undergo large angle scattering, in either the silicon detector or the copper detector mount, before reaching the scintillator and resulting in a coincidence trigger. Their energy deposition in the silicon detector is large enough to remove the event entirely from the expected energy range for the $^8\mathrm{B}(2^+) \rightarrow {}^8\mathrm{Be}(0^+)$ decay. As described below, we determined that positron summing reduced by 11.5% our efficiency for detecting ground-state decays.

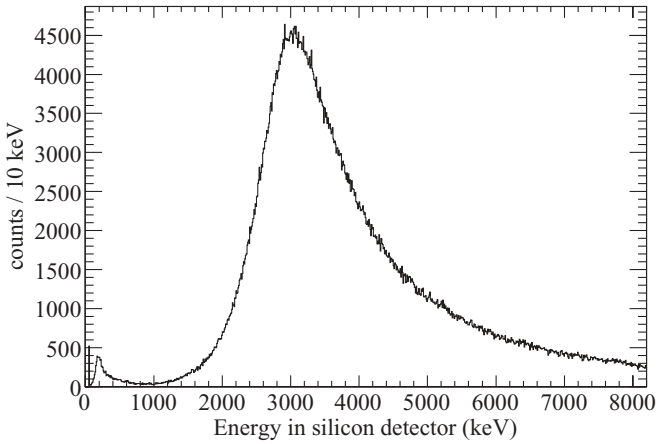

FIG. 5. Spectrum from the low-gain channel of the silicon detector, dominated by the $^8\mathrm{B}(2+) \rightarrow {}^8\mathrm{Be}(2+)$ decay. As discussed in the text, the 20-μm implantation depth limits the reliability of this spectrum to energies below 8 MeV.

III. DATA ANALYSIS

Following a series of commissioning runs, we accumulated 2.5×10^6 ^{8}B decay events over the course of two experimental runs. After selecting prompt events and applying cuts on the amplitude of the pulse in the scintillation counter, 2.0×10^6 events remained. The following discussion applies to both runs and is illustrated by examples from the second.

Following each run, the data in each of the silicon detector channels were corrected for gain drifts (the average correction was less than 0.3%), and the high-gain channel was calibrated using the information from the ^{133}Ba calibration data. A correction was also made for the α/γ ionization energy difference. No adjustments or calibrations were made to the scintillator or TAC spectra. The events of the final data set consisted of the corrected silicon-detector values and the corresponding raw scintillator and TAC values. This processing was applied separately to the data obtained using the ^{3}He and ^{4}He target gas. The ratio of random to true coincidence rate, in the energy region where the ground-state decay is expected, was found to be approximately 0.5% for both the ^{3}He and ^{4}He data. Since these data were subtracted to obtain the final data set, we made no further correction for accidental coincidences.

The spectrum from the low-gain channel, which is dominated by the $^8\mathrm{B}(2+) \rightarrow {}^8\mathrm{Be}(2+)$ decay, is shown in Fig. 5. Above about 8 MeV, Monte Carlo simulations indicate the spectrum is distorted by α particles that escape from the 20-μm implantation depth. Additional small distortions result from the scintillator threshold, which requires positrons over about 1.5 MeV, and consequently favors lower energy α particles. Finally, significant distortions result from backscattered positrons, many of which come from the copper cooling mount behind the detector. Presumably as a result of these distortions, which are examined in detail in Ref. [20], we were unable to get a useful R-matrix fit to this spectrum.

To determine the energy window in which the $^8\mathrm{B}(2^+) \rightarrow {}^8\mathrm{Be}(0^+)$ decay should be located, we begin by adding the recoil energy, distributed between 0 and 19.3 keV, to the total kinetic energy (91.8 keV) of the two α particles arising from ^{8}Be decay. To calculate the pulse-height defect of these α particles, we assume that the total energy is shared equally between the two α particles, thus giving a minimum and maximum kinetic energy for each α particle of 45.9 and 55.6 keV, respectively. The range of the pulse-height defect for these α particles was measured to be 4.5–7.5 keV. Thus, before accounting for the positron energy loss, the ground-state decay could be expected to appear between 9 and 15 keV lower than the sum of the decay and recoil energies. We convolve the calculated α-particle energy distribution with a Gaussian detector response with the typical 9-keV FWHM to produce an expected energy spectrum. The pulse-height defect shifts this spectrum downward between 9 and 15 keV. For each of these cases, we convolve the shifted spectrum with the spectrum of positron energy deposition calculated using the PENELOPE Monte Carlo package [21]. That spectrum corresponds to positrons emitted isotropically but depositing over 2.5 MeV in the scintillator. The spectrum has a peak at about 9 keV, corresponding to positrons that exited the silicon in the direction of the scintillator, but a long tail is produced by positrons that either backscattered from the copper mount or passed through significant thickness of silicon before a large-angle scattering into the scintillator. The final spectra, for the two limiting values of pulse-height defect, including positron summing, are illustrated in Fig. 6. We select the energy range of 75–120 keV for the region of interest. This region contains between 88.1% and 88.8% of the total events, depending on the assumed value for the pulse-height defect.

In this energy window, the rates of the two background processes in ^{8}Be, γ decay of excited states of ^{8}Be and α particles from the broad $^8\mathrm{B}(2^+) \rightarrow {}^8\mathrm{Be}(2^+)$ decay spectrum, were calculated to be two orders of magnitude below the sensitivity of this experiment.

The spectra obtained in the second experimental run, with ^{3}He (signal) and ^{4}He (background) in the gas cell, are shown in Fig. 7. The most striking feature is the large broad peak of coincident events, which was present in our data regardless of the target gas, and (at a slightly lower rate) even without the beam. The rate of events in this peak, 20 mHz, was relatively constant over a long time span ($\sim$4 years), regardless of the time between irradiations in the scattering chamber. We

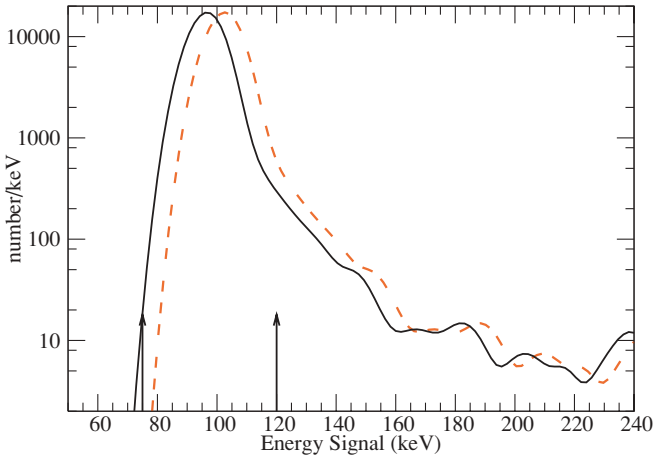

FIG. 6. (Color online) Monte Carlo simulations of silicon-detector response to decays to the ^{8}Be ground state for coincident events in scintillator and Si detectors. The initial α-particle energy spectrum is modified by recoil and positron energy summing. The two curves correspond to the two extreme values for the pulse-height defect. The arrows indicate the region chosen for searching for ground-state decays.

speculate that this peak is due to minimum-ionizing events from ambient radioactivity which pass through both the silicon and scintillator detectors. However, increased shielding and the addition of scintillator veto counters were not effective in reducing the rate.

Analysis of these events shows that they are dominated by low-energy scintillator events, and we can improve our experimental sensitivity by optimizing the scintillator minimum threshold. The optimum scintillator threshold was obtained by finding the minimum uncertainty in the difference of the time-normalized signal and background counts between 75 and 120 keV as a function of scintillator threshold. We maintained the average beam current in the measurements with ^{3}He and ^{4}He to be identical within 1%, so normalizing by time was equivalent to normalizing by integrated current. We

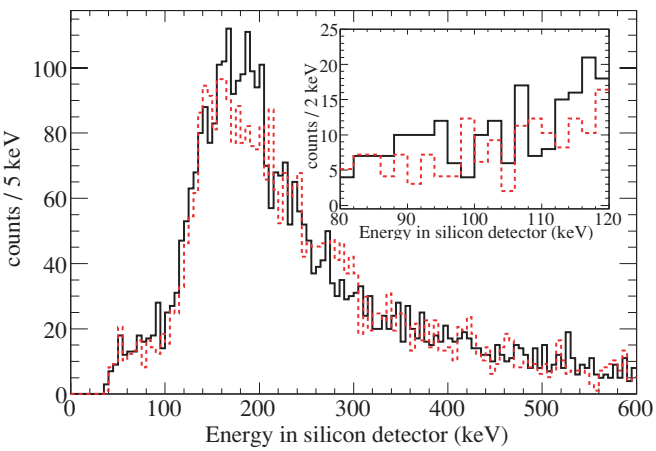

FIG. 7. (Color online) Measured signal (solid) and background (dashed) coincidence silicon-detector spectra for the high-gain channel with scintillator threshold applied.

subtracted the normalized background given by the ^{4}He data from the ^{3}He data.

Along with the background discussed above, additional background was present in the spectrum measured using the signal (^{6}Li + ^{3}He) reaction which was not present in the background (^{6}Li + ^{4}He) measurement. We hypothesize that this additional background resulted from positrons emitted from ^{8}B implanted on surfaces other than the silicon detector. These positrons may pass through both the silicon and scintillator detectors and result in a false coincidence trigger and a continuum of events in the energy spectrum.

Since this background had the same general shape as the larger background observed with the beam off or with ^{4}He in the gas cell, we assume it is composed primarily of a spectrum of the same shape, but we will allow for the possibility of additional background in the energy range of interest. Such a background would be identified by additional counts in the spectrum adjacent to the energy window for the ground-state decay.

To account for the first part of this background, we parametrized the shape of the background spectrum by fitting the measured background energy spectrum from 50 to 400 keV, as shown in the first plot of Fig. 8. The parametrization function consisted of a Landau distribution and a linear term. Holding the parameters from the background fit fixed and allowing for a free multiplicative normalization factor, the parametrization function was then fit to the signal energy spectrum over an energy window of 140–400 keV, as shown in the second plot of Fig. 8. Excluding the area around the ^{8}B(2^+) $\rightarrow$ ^{8}Be(0^+) decay signature window ensured that the normalization was not influenced by counts in that window. The number of expected background events in the signal region was obtained by integrating the fit function over the energy region of interest. To identify the second part of this background, the excess of counts above this calculated background was computed in the signal window (75–120 keV) and two adjacent energy windows (50–75 and 120–140 keV).

The excess of net counts above the fit background in all three energy windows confirms the second background, which is not present in the ^{4}He measurements from which the initial background estimates are derived. To account for this additional background, we interpolated between the two adjacent windows to determine the number of background events in the primary energy window. We then subtracted this background from the total number of excess events obtained from the difference between the data and the fit, to get the net excess of signal events. To account for the loss of efficiency due to positron backscattering, we multiplied the net excess of counts by 1.13. The branching ratio was calculated by dividing the corrected net excess number of counts by the total number of detected coincident events. The results of this analysis are given in Table I.

The data from the two experimental runs, given in Table I, combined with the total of 1.96×10^6 decays collected, yields a branching ratio for the ^{8}B(2^+) $\rightarrow$ ^{8}Be(0^+) decay of $(2.6 \pm 3.3) \times 10^{-5}$. This result is consistent with no measured signal and corresponds to an upper limit on the branching ratio of 7.3×10^{-5} at a 90% confidence level.

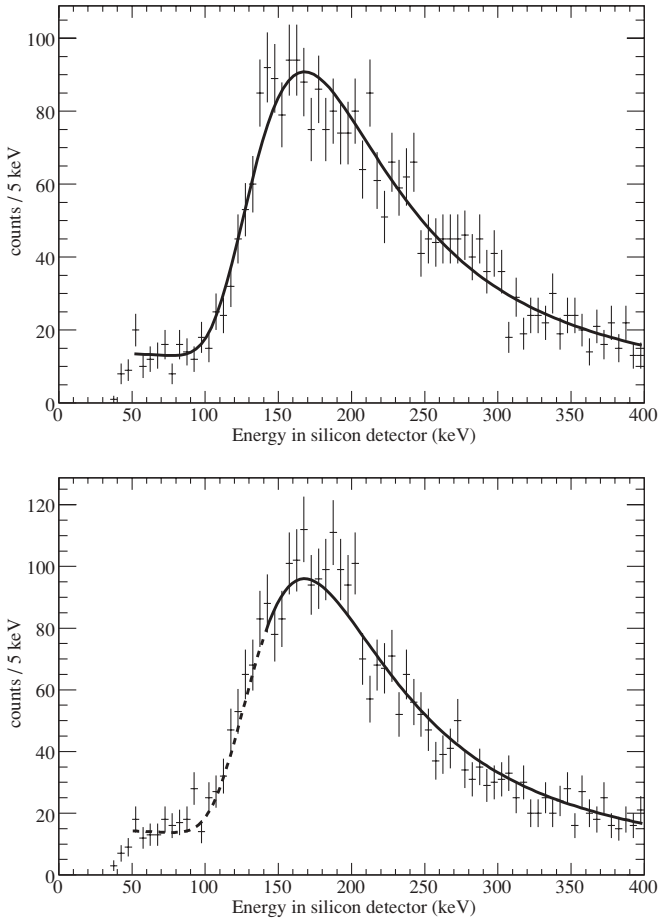

FIG. 8. Data from the second experimental run. The upper plot is the data measured with ^{4}He in the gas cell, with the fit to this background. The lower plot is the data measured with ^{3}He in the gas cell, with a fit to the data above 140 keV using the parameters obtained from the background spectrum, but allowing for an adjustable multiplicative normalization. The dashed range of the lower curve denotes the energy region of interest for signal extraction.

IV. THEORETICAL ESTIMATE OF BRANCHING RATIO

One published estimate [6,7] of the $^8\mathrm{B}(2^+) \rightarrow {}^8\mathrm{Be}(0^+)$ decay rate is based on the conserved vector current (CVC), which relates the vector contribution to the β-decay rate to the γ decay of the 16-MeV isobaric analog state of ^{8}Be [22]. These calculations do not consider the contribution of the axial matrix element to the decay rate. Another estimate [5] is based on several different model calculations of the axial-vector second forbidden contribution to the decay to the first excited state of ^{8}Be. Those authors suggest that based on the similarity of the intrinsic wave functions of the ground and first excited states of ^{8}Be, these calculations can be applied to the ground-state decay, and they find a branching ratio of approximately 3×10^{-6}. However, since no experimental information is available to constrain the contribution of the axial matrix element to the transition, a strong axial contribution cannot simply be ruled out.

In this section, we discuss our application of the framework developed by Walecka [23,24] and Donnelly and Haxton [25] for calculating the rates of electromagnetic and semileptonic processes. The details of the calculations discussed in this section are specific to the $^8\mathrm{B}(2^+) \rightarrow {}^8\mathrm{Be}(0^+)$ decay. Our application of this framework is described in detail in Ref. [20].

A. Shell model estimate

The rate of the $^8\mathrm{B}(2^+) \rightarrow {}^8\mathrm{Be}(0^+)$ second forbidden ^{8}B decay can be expressed in terms of kinematic variables and multipole matrix elements, using the formalism in Ref. [23]. This formalism is quite general, as it includes all multipoles and leaves the local weak current unspecified—so that exchange-current or other corrections to the usual one-body operators can be included. The transition of interest involves an angular momentum change from $J = 2$ to $J = 0$, with no change in parity. The relevant operators, expanded in the long-wavelength limit (since $qR \ll \hbar c$), are given in terms of the vector and axial vector currents, $\mathbf{J}(\mathbf{x})$ and $\mathbf{J}_5(\mathbf{x})$ [24]. These operators, $\hat{M}_2(q)$, $\hat{T}_2^{\mathrm{el}}(q)$, and $\hat{T}_2^{\mathrm{mag5}}(q)$, are the rank-two charge and transverse electric projections of the vector current and the transverse magnetic projection of the axial current, respectively.

The vector current appearing in $\hat{T}_2^{\mathrm{el}}$ has a one-body part and two-body exchange-current corrections, both of which are of the order (v_{nuc}/c). A direct calculation of the important exchange-current corrections would be difficult to do precisely in a model calculation. Fortunately, under CVC and in the long wavelength limit, it is possible to rewrite matrix elements of $\hat{T}_2^{\mathrm{el}}$ in terms of those of $\hat{M}_2$ through Siegert's theorem [26]. The benefit of this substitution is that the one-body charge operator is of order $(v_{\mathrm{nuc}}/c)^0$, while two-body corrections to this operator are of order $(v_{\mathrm{nuc}}/c)^2$. Thus Siegert's theorem allows one to deal with a simpler operator that can be well approximated by its one-body form. The β-decay rate then can be written in terms of $\hat{M}_2(q)$ and $\hat{T}_2^{\mathrm{mag5}}(q)$. As discussed below, the matrix element of the Coulomb operator can be taken from the isobaric analog γ-decay transition. Thus the nuclear-structure dependence of our result is effectively isolated in a single matrix-element ratio, $\langle \hat{T}_2^{\mathrm{mag5}} \rangle / \langle \hat{M}_2 \rangle$.

B. Calculation of the density matrix

For weak and electromagnetic interactions, the interaction can be well approximated by considering only the one-body interaction [25]. We define $|\alpha\rangle$ and $|\beta\rangle$ as complete single-particle wave functions, and we also define $||\alpha|\rangle$ and $||\beta|\rangle$ as the reduced (in angular momentum and isospin) forms of these single-particle wave functions, i.e., $|n, l, j, t\rangle$. We can then write a many-body multipole reduced matrix element $\langle J_f T_f \| \hat{\mathcal{O}}_{JT} \| J_i T_i \rangle$ as the sum of single-particle matrix elements $\langle |\alpha| \| \mathcal{O}_{JT} \| |\beta| \rangle$ multiplied by the density matrix elements $\psi_{\alpha\beta}$, as defined in Ref. [25].

For the $^8\mathrm{B}(2^+) \rightarrow {}^8\mathrm{Be}(0^+)$ transition, the coefficients for the density matrix were obtained from p-shell wave functions calculated using the GLASGOW shell model [27] with the Cohen-Kurath (8–16)2BME interaction [28]. The numerical values are given in Table II.

TABLE I. Number of measured events and predicted background in the spectrum obtained with ^{3}He gas in the cell. Both experimental runs are combined.

Energy window (keV)	Events from data	Bkg. events from fit	Net remaining	Interpolated bkg.	Net excess
50–75	282±16.8	255.7±16.0	26.2±23.2	–	–
75–120	661±25.7	575.4±24.0	85.6±35.2	40.4±44.4	45.2±56.7
120–140	589±24.2	573.9±23.8	15.1±34.0	–	–

C. Single-particle matrix elements

The single-particle operators relevant to this calculation are defined in terms of spherical Bessel functions j_J and scalar and vector spherical harmonics $Y_J^{M_J}$ and $\mathcal{Y}_{JL1}^{M_J}$ [25]:

$$M_J^{M_J}(q\mathbf{x}) \equiv j_J(qx)Y_J^{M_J}(\Omega_x), \tag{1}$$

$$\Sigma_J^{M_J}(q\mathbf{x}) \equiv j_J(qx)\mathcal{Y}_{JJ1}^{M_J}(\Omega_x)\cdot\boldsymbol{\sigma}. \tag{2}$$

The matrix elements of these operators can be expanded in a harmonic oscillator basis and expressed as functions of the form [25]

$$\langle n_f(l_f\ \tfrac{1}{2})j_f\|T_J(q\mathbf{x})\|n_i(l_i\ \tfrac{1}{2})j_i\rangle = \sqrt{\frac{1}{4\pi}}y^{(J-2)/2}e^{-y}p(y), \tag{3}$$

where $T_J(q\mathbf{x})$ is a generic single-particle operator reduced in spin/isospin, $y \equiv (\frac{1}{2}qb)^2$, $b = 1.787$ fm is the oscillator parameter [30], and $p(y)$ is a polynomial of finite order in y, as tabulated in Ref. [25].

Folding the matrix elements of Ref. [25] with the Cohen-Kurath density matrix yields

$$\langle J_f\|\hat{M}_2\|J_i\rangle = \tfrac{-0.23F_1}{\sqrt{4\pi}}\left(-\tfrac{4y}{3}\right)\exp(-y), \tag{4a}$$

$$\langle J_f\|\hat{T}_2^{\mathrm{mag5}}\|J_i\rangle = \tfrac{0.04F_A\sqrt{6}}{\sqrt{4\pi}}\left(-\tfrac{2y}{3}\right)\exp(-y), \tag{4b}$$

where $F_1 = 1.0$ and $F_A = 1.26$ are the single-nucleon charge and axial-vector couplings.

While the $\hat{M}_2$ and $\hat{T}_2^{\mathrm{mag5}}$ matrix elements have identical momentum dependence, a suppression of the $\hat{T}_2^{\mathrm{mag5}}$ matrix element is caused by the cancellation to 20% in the sum of the density matrix elements:

$$\psi_{\frac{3}{2}\frac{1}{2}} + \psi_{\frac{1}{2}\frac{3}{2}} = 0.17 - 0.21 = -0.04. \tag{5}$$

The uncertainty of this model dependence is difficult to quantify, and therefore we unfortunately cannot be assured that this result reflects the true strength of the axial contribution to this decay. Despite this, we are now able to obtain the β-decay rate for the $^8\mathrm{B}(2^+) \rightarrow {}^8\mathrm{Be}(0^+)$ decay. We find that the vector contribution dominates, and the resulting branching ratio is 6.1×10^{-5}.

TABLE II. Calculated density matrix elements for $1p$-shell transitions for $^8\mathrm{B}(2^+) \rightarrow {}^8\mathrm{Be}(0^+)$ decay, using the Cohen-Kurath (8-16)2BME interaction [28] and calculated using code obtained from Ref. [29]. The notation $a \rightarrow b$ denotes the density matrix element ψ_{ab}, which connects the single-particle states with $j_i = a$ and $j_f = b$.

Transition	Density matrix coefficient
$\frac{1}{2} \rightarrow \frac{3}{2}$	−0.206564
$\frac{3}{2} \rightarrow \frac{1}{2}$	+0.168713
$\frac{3}{2} \rightarrow \frac{3}{2}$	−0.608563

D. Vector contribution derived from electromagnetic rate

Since our shell model calculation showed dominance of the vector contribution to the decay, it is useful to compare that result with the value implied by measurements of isobaric analog electromagnetic transitions. The doublet in ^{8}Be at 16.6/16.9 MeV is composed of a $T = 0$ state mixed with the $T = 1$ isobaric analog state of the ^{8}B ground state. The reduced strengths for the $E2$ transition from these states to the ground state of ^{8}Be are $B(E2)_{16.6} = 0.068 \pm 0.024\, e^2\ \mathrm{fm}^4$ and $B(E2)_{16.9} = 0.075 \pm 0.013 e^2\ \mathrm{fm}^4$ [22]. Because of the ambiguity in the phase of the matrix elements, decomposing the measured transition strengths into isovector and isoscalar components gives two results: either $B(E2)_{\mathrm{IV}} = 0.00 \pm 0.03$ and $B(E2)_{\mathrm{IS}} = 0.14 \pm 0.03\, e^2\ \mathrm{fm}^4$; or alternatively, $B(E2)_{\mathrm{IV}} = 0.14 \pm 0.03$ and $B(E2)_{\mathrm{IS}} = 0.00 \pm 0.03\, e^2\ \mathrm{fm}^4$. We will henceforth use the maximum $(0.14 + 0.03 = 0.17\, e^2\ \mathrm{fm}^4)$ and minimum (0.0) values for $B(E2)_{\mathrm{IV}}$ to constrain the β-decay transition rate.

The rate of the nuclear electromagnetic transition rate in terms of the multipole operators defined in the previous section is [24]

$$\omega_\gamma = \frac{8\pi\alpha k_\gamma}{2J_i+1}|\langle f\|\hat{T}_J^{\mathrm{el}}\|i\rangle|^2, \tag{6}$$

where ω_γ is the transition rate per unit time, k_γ is the γ-ray momentum, α is the fine structure constant, J is the angular momentum change in the transition, and J_i is the initial spin of the nucleus. As with the β-decay expression, we can rewrite this in terms of the $\hat{M}_2$ matrix element using Siegert's theorem [26] and substituting $J = J_i = 2$,

$$\omega_\gamma = \frac{3}{2}\frac{8\pi\alpha}{5}\frac{(E_i - E_f)^2}{k_\gamma}|\langle f\|\hat{M}_2\|i\rangle|^2. \tag{7}$$

The energy released in the isovector decay is 16.80 MeV [22], and the corresponding decay rate from Eq. (7) yields a $B(E2)$ value of 0.55 e^2 fm^4 for the transition, using the $\hat{M}_2$ matrix element obtained in the previous section. For this calculation to match the measured $B(E2) = 0.17\, e^2\ \mathrm{fm}^4$, the matrix element must be reduced by a factor of 1.8. To incorporate the second $[B(E2)_{\mathrm{IV}} = 0]$ constraint, we simply set $M_2 = 0$ in the β-decay calculation.

If we assume the maximum possible strength of the vector matrix element from the γ-decay measurement, we obtain a transition rate of $1.8 \times 10^{-5}\text{s}^{-1}$. On the other hand, if we assume that the vector matrix element does not contribute, the transition rate is reduced to $9.1 \times 10^{-7}\text{s}^{-1}$. The respective branching ratios for these cases are 2.0×10^{-5} and 1.0×10^{-6}.

V. CONCLUSIONS

An accurate measurement of or limit on the $^8\text{B}(2^+) \rightarrow {}^8\text{Be}(0^+)$ β-decay branching ratio is of importance for the current generation of solar neutrino measurements. To the best of our knowledge, this work is the first published attempt at the measurement of the $^8\text{B}(2^+) \rightarrow {}^8\text{Be}(0^+)$ decay branching ratio.

Our measurement of the $^8\text{B}(2^+) \rightarrow {}^8\text{Be}(0^+)$ β-decay transition centers on the detection of the two low-energy α particles from the breakup of ^{8}Be. A significant challenge to this measurement is the characterization of the response of our silicon detector to low-energy α particles. In light of this, we have done two experiments to determine our detector response. The first measurement involved directly implanting α particles with kinetic energy between 86 and 453 keV into our detector, while simultaneously measuring the detector dead layer. The second measurement involved the implantation of ^{12}N, which is unstable to β-delayed 3α decay. The results from both of these measurements verify that the tabulated nuclear stopping powers for α particles in silicon are reasonably valid for the range of energies we are considering. However, the directly implanted low-energy α-particle measurements indicates that the uncertainty on the tabulated values may be larger than predicted.

Using the measurements and techniques described above, we have measured the $^8\text{B}(2^+) \rightarrow {}^8\text{Be}(0^+)$ decay branching ratio to be $(2.6 \pm 3.3) \times 10^{-5}$. This measurement is consistent with zero and can be used to place an upper limit on the branching ratio of 7.3×10^{-5} at the 90% confidence level. At this level, the $^8\text{B}(2^+) \rightarrow {}^8\text{Be}(0^+)$ decay branch is not a significant background to measurements of the spectral shape of solar ^{8}B neutrinos and the solar hep neutrino flux. Our calculation of the $^8\text{B}(2^+) \rightarrow {}^8\text{Be}(0^+)$ decay rate gives a branching ratio of 6.1×10^{-5}, using values for the vector and axial-vector matrix elements obtained from the shell model. The model-dependent axial term in our calculation may be quite uncertain. We find a branching ratio range of 1.0×10^{-6} to 2.0×10^{-5}, based on the values for the vector matrix element obtained from the experiment of Ref. [22] along with the axial-vector matrix element obtained from the shell model. The values are all consistent with our measured value.

ACKNOWLEDGMENTS

The authors thank Wick Haxton for his assistance with the theoretical aspects of this work and the CENPA technical staff including John Amsbaugh, Greg Harper, Mark Howe, and Doug Will, all of whom contributed extraordinary amounts of time and effort in support of the experimental measurements. We also thank Eric Adelberger, Manojeet Bhattacharya, Jason Detwiler, Alejandro Garcia, Seth Hoedl, and John Wilkerson for their wealth of ideas and insights. Finally, work by Matthias Gohl, Shuje Uehara, Ashley Batchelor, Christy McKinley, Patrick Peplowski, and many other UW tandem crew members was crucial to carrying out this work. This research was partially supported by DOE Grant DE-FG03-97ER41020.

[1] W. T. Winter, S. J. Freedman, K. E. Rehm, and J. P. Schiffer, Phys. Rev. C **73**, 025503 (2006).
[2] M. Bhattacharya, E. G. Adelberger, and H. E. Swanson, Phys. Rev. C **73**, 055802 (2006).
[3] C. E. Ortiz, A. Garcia, R. A. Waltz, M. Bhattacharya, and A. K. Komives, Phys. Rev. Lett. **85**, 2909 (2000).
[4] B. Aharmim *et al.* (SNO Collaboration), Astrophys. J. **653**, 1545 (2006).
[5] R. Tribble and G. Garvey, Phys. Rev. C **12**, 967 (1975).
[6] C. E. Ortiz, Ph.D. thesis, University of Notre Dame, 2000 (unpublished).
[7] A. Garcia (private communication), confusion of units in a quoted equation caused an error of 10^{-6} in the estimate given in Ortiz's Ph.D. thesis.
[8] Hamilton Precision Metals, www.hpmetals.com.
[9] U. Rohrer, PSI Graphic Transport Framework based on a CERN-SLAC-FERMILAB version by K. L. Brown *et al.*, http://people.web.psi.ch/rohrer_u/trans.htm.
[10] U. Rohrer, PSI Graphic Turtle Framework based on a CERN-SLAC-FERMILAB version by K. L. Brown *et al.*, http://people.web.psi.ch/rohrer_u/turtle.htm.
[11] J. F. Amsbaugh, G. C. Harper, A. W. Myers, T. D. Van Wechel, and D. I. Will, CENPA Annual Report, 2005 (unpublished), p. 88.
[12] Hamamatsu, http://jp.hamamatsu.com/en/index.html.
[13] H. P. Mumm, A. Garcia, L. Grout, M. A. Howe, L. P. Parazzoli, R. G. H. Robertson, K. M. Sundqvist, J. F. Wilkerson, S. J. Freedman, B. K. Fujikawa *et al.*, Rev. Sci. Instrum. **75**, 5343 (2004).
[14] Wiener, Plein & Baus, Ltd., http://www.wiener-us.com/cc32.htm.
[15] D. Visser and K. Swartz, JAM data acquisition system, http://sourceforge.net/projects/jam-daq.
[16] M. A. Howe, G. A. Cox, P. J. Harvey, F. McGirt, K. Rielage, J. F. Wilkerson, and J. M. Wouters, IEEE Trans. Nucl. Sci. **51**, 874 (2004).
[17] ICRU, Tech. Rep. 31, 1979 (International Commission on Radiation Units, 7910 Woodmont Ave., Washington, DC 20014) (unpublished).
[18] M. J. Berger, J. S. Coursey, M. A. Zucker, and J. Chang, "ESTAR, PSTAR, and ASTAR: Computer programs for calculating stopping-power and range tables for electrons, protons, and helium ions," 2005, an online database with machine-readable stopping power data from ICRU Tech. Rep. 49, 1993, http://physics.nist.gov/Star.
[19] J. F. Ziegler, SRIM: Stopping and Ranges of Ions in Matter, www.srim.org.
[20] M. K. Bacrania, Ph.D. thesis, University of Washington, 2006 (unpublished).

[21] J. Sempau, E. Acosta, J. Baro, J. M. Fernńdez-Varea, and F. Salvat, Nucl. Instrum. Methods B **132**, 377 (1997).
[22] L. De Braeckeleer *et al*., Phys. Rev. C **51**, 2778 (1995).
[23] J. D. Walecka, in *Muon Physics*, edited by V. W. Hughes and C. S. Wu (Academic, New York, 1975), Vol. II, Chap. 2, p. 113.
[24] J. D. Walecka, *Theoretical Nuclear and Subnuclear Physics*, 2nd ed. (World Scientific, Singapore, 2004).
[25] T. W. Donnelly and W. C. Haxton, At. Data Nucl. Data Tables **23**, 103 (1979).
[26] A. J. F. Siegert, Phys. Rev. **52**, 787 (1937).
[27] R. R. Whitehead, A. Watt, B. J. Cole, and I. Morrison, Adv. Nucl. Phys. **9**, 123 (1977).
[28] S. Cohen and D. Kurath, Nucl. Phys. **73**, 1 (1965).
[29] W. C. Haxton (private communication).
[30] J. Dubach and W. C. Haxton, Phys. Rev. Lett. **41**, 1453 (1978).